Electronic Supplementary Material (ESI) for Journal of Materials Chemistry A.

Supporting Information

Basal Plane Activation in Monolayer $MoTe_2$ for Hydrogen Evolution Reaction via Phase Boundaries

Yiqing Chen, Pengfei Ou, Xiaohan Bie, Jun Song*

Department of Mining and Materials Engineering, McGill University, Montreal H3A 0C5, Canada

Corresponding Author: *E-mail: jun.song2@mcgill.ca.

S1. Benchmark studies on nanoribbon models

As stated in the manuscript, we have performed benchmark calculations to ensure that our results are not affected by edge-edge or edge-boundary interactions. We evaluated the formation energies (E_f) of phase boundaries and the Gibbs free energy of adsorption ΔG_H as functions of the number (n) of unit cells in each phase. Fig. S1 shows some sample results from our benchmark calculations for the phase boundary $ZZ_{Mo} - \beta - T| +$. As seen from Fig. S1, the simulation cell should have no less than 8 unit cells between the edge and boundary to avoid artificial effects. In our calculations, we used $n = 10$.

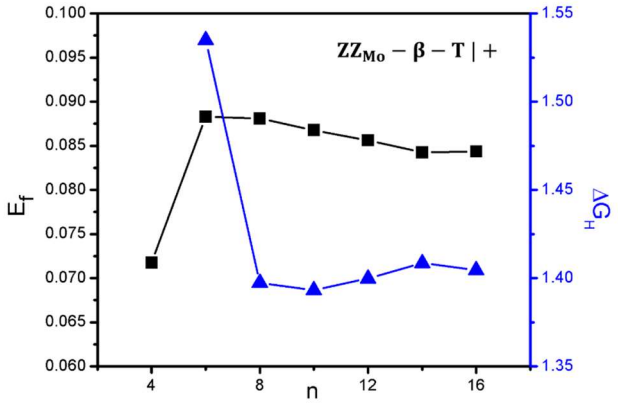

Fig. S1 Benchmark studies of the possible effect, induced by edge-edge and edge-boundary interactions, on the formation energy E_f of the phase boundary $ZZ_{Mo} - \beta - T| +$ and the Gibbs free energy of adsorption ΔG_H as functions of the number (n) of unit cells in each phase.. E_f was calculated under Te-rich condition ($\mu_{Te} = -3.14\ eV$), and the hydrogen coverage in benchmark studies was set as 1.

S2. The effect of exchange-correlation functional on the electronic structure calculations

Fig. S2 below shows the total DOS of pristine 2H and 1T' $MoTe_2$, obtained from calculations using generalized gradient approximation (GGA-PBE) [1] and hybrid exchange-correlation functional (HSE06) [2]. We can see from the figure that for 2H or 1T' $MoTe_2$, the DOS plots from GGA-PBE and HSE06 are quite similar, which indicates that our conclusion will not change even if the calculations are done based on other functionals.

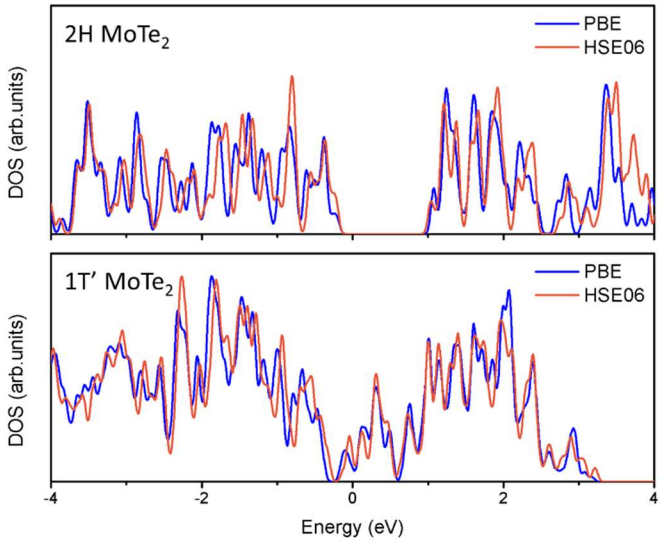

Fig. S2. Total density of states (DOS) of pristine 2H $MoTe_2$ and pristine 1T' $MoTe_2$, obtained from calculations using GGA-PBE [1] (red) and HSE06 [2] (blue) functionals.

S3. Details of formation energy calculations of zigzag phase boundaries

Nanoribbon-like structures have been employed in other studies to explore the stabilities of zigzag phase boundaries for TMDCs [3, 4]. In the present study, we adopt this method to calculate

the formation energies of zigzag phase boundaries in $MoTe_2$. The total energy of a phase boundary structure, E_T, can be obtained as follows:

$$E_T = N_{Mo}\mu_{Mo} + N_{Te}\mu_{Te} + L\left(\sigma_H + \sigma_{T'} + E_f\right) \quad \text{(S1)}$$

where the parameters N_{Mo}, N_{Te}, L and E_T are readily obtained from DFT calculations, and μ_{Te} has a range of $[-3.54, -3.14]$ eV. In order to calculate the formation energy E_f, we need to determine the two parameters, σ_H and $\sigma_{T'}$. Here, we construct a 2H $MoTe_2$ nanoribbon and a 1T' $MoTe_2$ nanoribbon, as shown in Fig. S3(a)-(b). 2H $MoTe_2$ nanoribbon consists of two edges, i.e. β and α, and its total energy E_H can be expressed as:

$$\sigma_{H_\alpha} + \sigma_{H_\beta} = \frac{E_H - N_{Mo}\mu_{Mo} - N_{Te}\mu_{Te}}{L} \quad \text{(S2)}$$

Since β and α are inseparable in the simulation cell, a series of triangle quantum dots are further used to calculate the edge β, as shown in Fig S3(c). Then we could have the relationship between the total energy $E_{tri}(n)$ and quantum dot n as:

$$f(n) = E_{tri}(n) - \frac{n(n+1)}{2}\mu_{MoTe_2} = \left(2\mu_{Te} + 3\sigma_{H_\beta}\right)n + 3E_{cor} + 2\mu_{Te} \quad \text{(S3)}$$

where E_{cor} is the energy of three corners of the quantum dot. As shown in Fig. S3(d), by fitting the plot of $f(n)$, the edge energy σ_{H_β} can be obtained from the slope. Then the edge energy σ_{H_α} can be calculated from Eq. S2.

For 1T' $MoTe_2$ nanoribbon, same edges can be constructed at both ends of the phase boundary structures in a simulation cell. Therefore, its total energy E_T can be expressed as:

$$\sigma_{T'} = \frac{E_{T'} - N_{Mo}\mu_{Mo} - N_{Te}\mu_{Te}}{2L} \quad \text{(S4)}$$

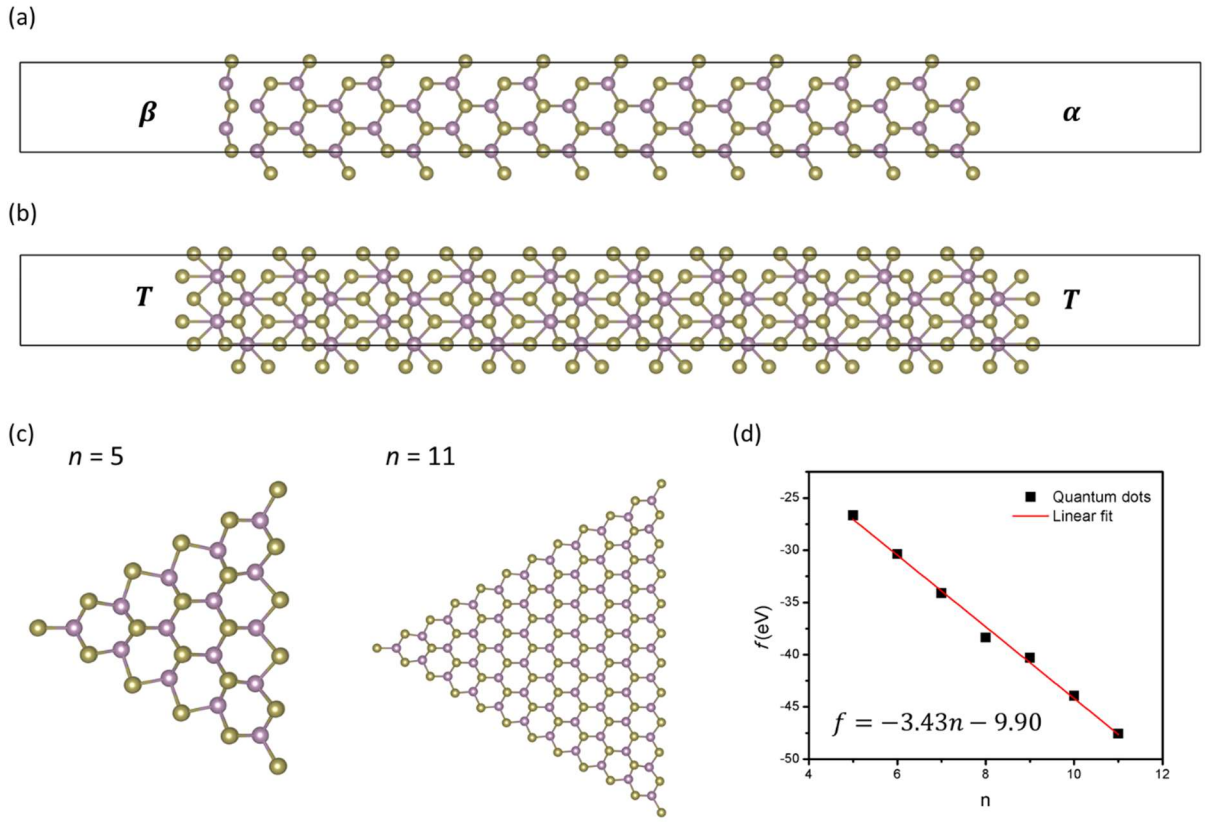

Fig. S3. (a), (b) Simulation cells of 2H $MoTe_2$ nanoribbon and 1T' $MoTe_2$ nanoribbon respectively. (c) Top views of quantum dot n, using $n = 5$ and $n = 11$ as representatives. (d) Linear fitting of $f(n)$ (see Eq. (S3)) as a function of n.

S4. Local bond variation at the phase boundary

The formation energy of a phase boundary is strongly correlated with the local bond distortion at the boundary. The bond distortion for each phase boundary is evaluated by comparing the Mo-Te bond lengths at the phase boundary with those in the pristine $MoTe_2$. As shown in Fig. S4(b), from $ZZ_{Mo} - \beta - C| +$, $ZZ_{Mo} - \beta - C| +$ to $ZZ_{Te} - \beta - C| +$ boundary, the formation energy increases with the increased variation in Mo-Te bond lengths.

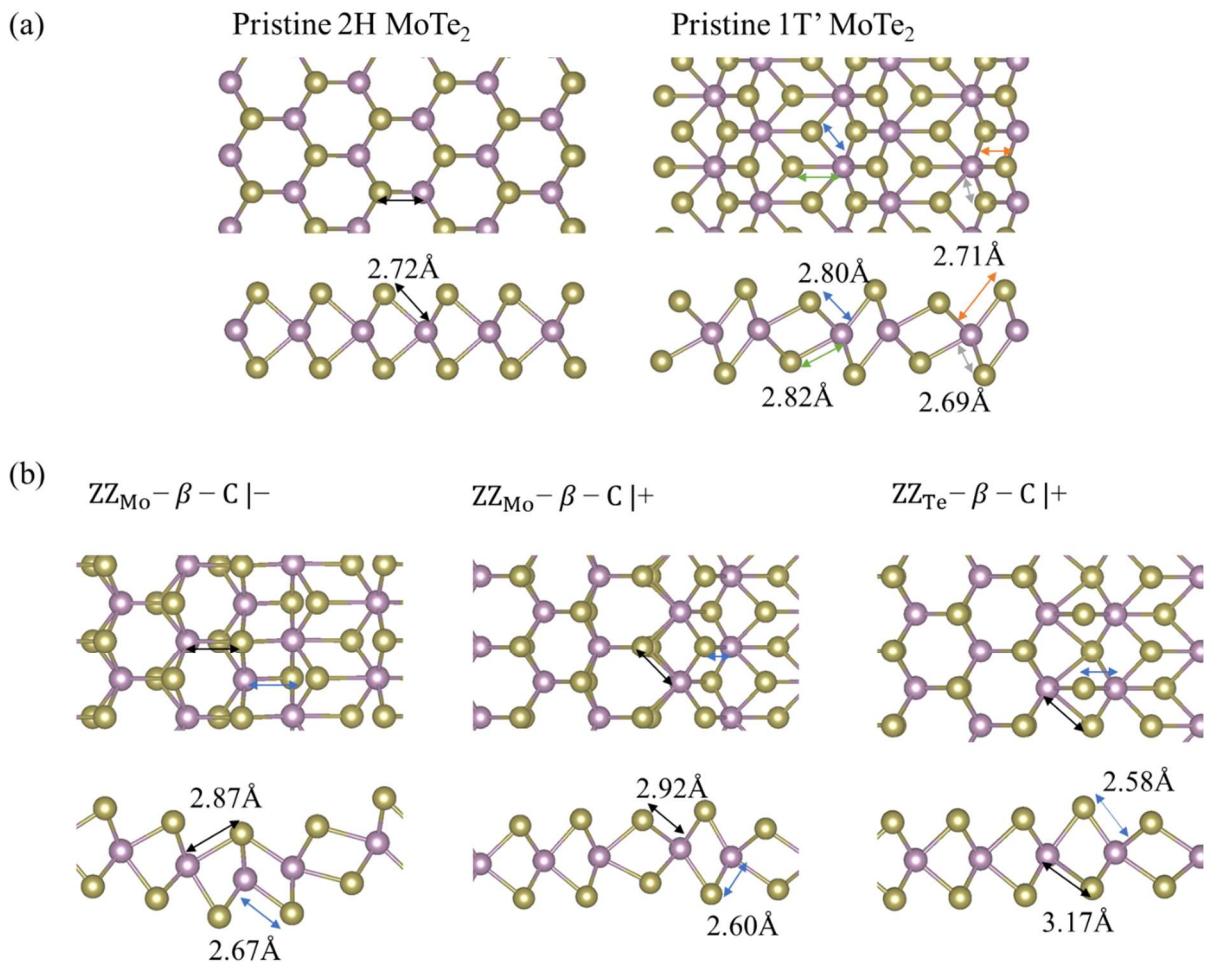

Fig. S4. (a) Top and side views of pristine 2H and 1T' $MoTe_2$, where the black arrow indicates the Mo-Te bond length of pristine 2H $MoTe_2$, while blue, green, orange and yellow arrows indicate various Mo-Te bonds length of pristine 1T' $MoTe_2$. (b) Top and side views of representative ZZ phase boundaries. For each phase boundary configuration, black and blue arrows indicate the longest and shortest Mo-Te bonds at the phase boundary, respectively.

S5. Thermal stability of phase boundaries at room temperature

To examine the thermal stability of the phase boundaries, we have performed a series of finite-temperature ab-initio molecular dynamics (AIMD) simulations in which phase boundaries were equilibrated at 300K (with isothermal-isobaric (NPT) ensemble with a 1.0 fs time step). In general we found that the system reaches equilibrium after 500fs. Fig. S5 below shows some benchmark results for the two low-energy boundaries, i.e., $ZZ_{Mo}-\alpha-C|-$ and $ZZ_{Mo}-\beta-$

$T|+$. As seen in Fig. S5(b), the structures of these two boundaries remain stable at 300K, except for lattice vibration due to thermal fluctuation (as compared to the configurations at 0K, c.f., Fig. 1(c)). Additional benchmark AIMD simulations have also been performed at higher temperature of 600K, at which the boundaries are also found to remain stable.

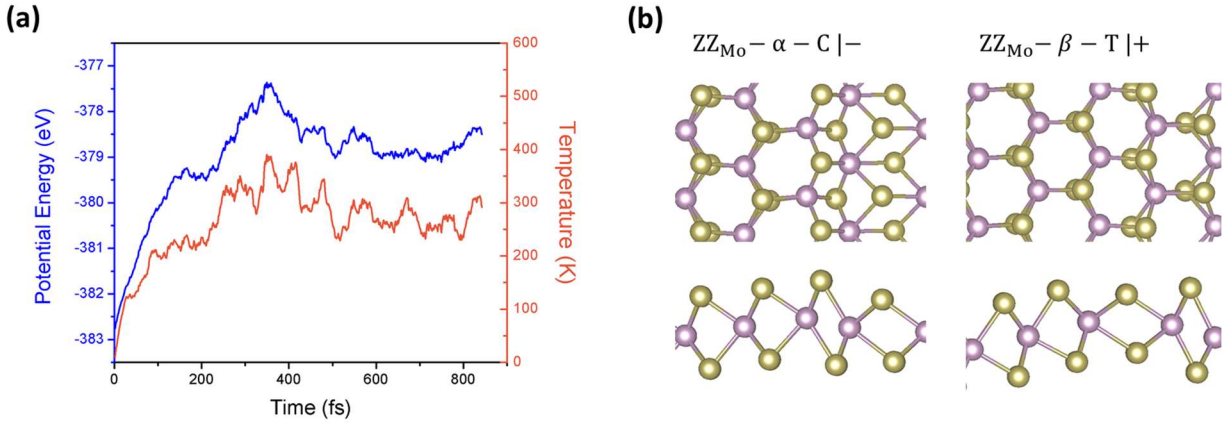

Fig. S5. (a) The potential energy (blue curve, left vertical axis) and temperature (red curve, right vertical axis) of $MoTe_2$ boundaries with simulation time. (b) Snapshots of configurations of $ZZ_{Mo}-\alpha-C|-$ and $ZZ_{Mo}-\beta-T|+$ boundaries at room temperature (300K).

S6. Hydrogen adsorption at HL sites

The hydrogen adsorption configurations at HL sites for phase boundaries and pristine structures are shown in Fig. S6. In the case of phase boundaries, hydrogen is adsorbed in the middle of the three-atom-thick monolayer surrounded by three Mo atoms. In contrast, for the pristine $MoTe_2$, the hydrogen atom tends to be adsorbed on Te atoms on the surface rather than the Mo atoms in the middle layer. To investigate the degree of activation of Mo atoms by the formation of phase boundaries, we manually put the hydrogen directly into the middle of the hollow site for the case of pristine $MoTe_2$, so that it will not be adsorbed on the Te atom from the top layer. The adsorption site is denoted as Pristine HL. As shown in Table S1, in comparison with the results for other HL sites, $\Delta G_{H-Pristin\ \ HL}$ shows a value of 0.74 eV, much larger than the values for the hollow sites in the phase boundary region. Therefore, the activation of Mo atoms after the formation of phase boundaries leads to the adsorption into the HL sites.

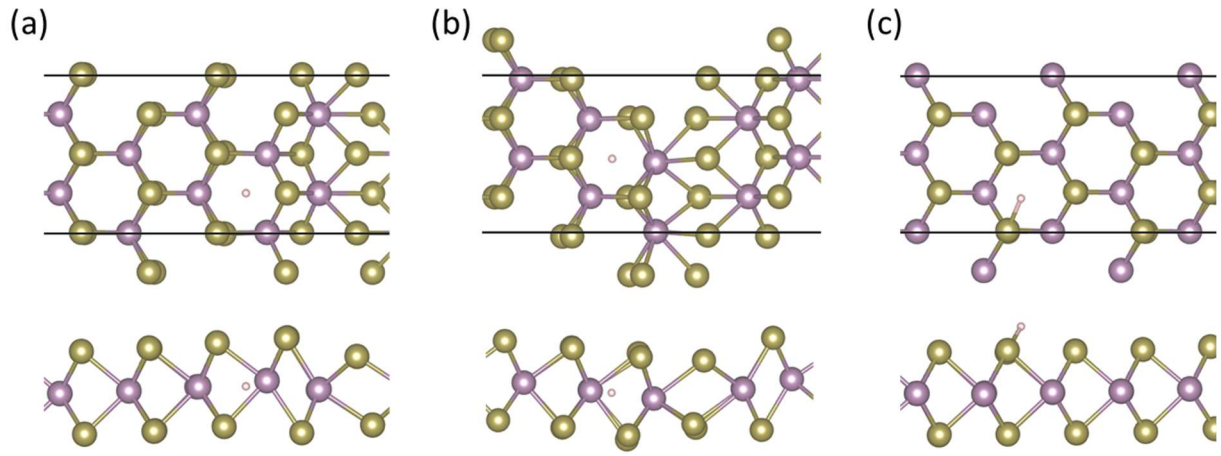

Fig. S6. (a), (b), (c) The hydrogen adsorption configurations for HL1, HL2 and the pristine $MoTe_2$.

Table S1. ΔG_H values for different hollow sites.

Site	ΔG_H (eV)
HL1	-0.10
HL2	0.19
Pristine	1.79
Pristine HL	0.74

S7. Adsorption sites of pristine 2H and 1T' $MoTe_2$

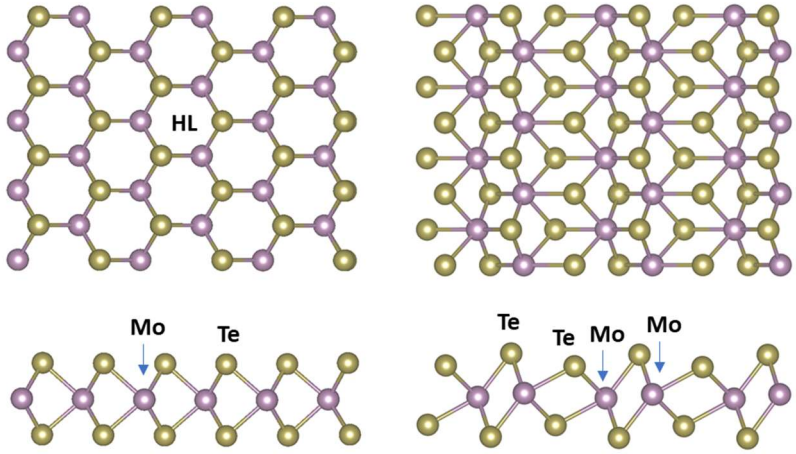

Fig. S7. Adsorption sites of pristine 2H and 1T' $MoTe_2$. Adsorption sites are categorized into hollow (HL), Mo, and Te sites respectively, and labelled accordingly.

S8. Free energy diagrams for the hydrogen evolution at the phase boundaries

The HER is a multistep electrochemical process. What we have calculated in the manuscript is the first step, i.e. Volmer step, where the first hydrogen is adsorbed onto a $MoTe_2$ catalyst, describing by $H^+ + e^- + * \rightarrow H^*$. The second step is the release of H_2 molecules, which is achieved by either the Heyrovsky ($H^* + H^+ + e^- \rightarrow H_2 + *$) or Tafel ($2H^* \rightarrow H_2 + 2*$) reaction. To determine the HER pathway on $MoTe_2$ phase boundaries, we calculated the free energy diagrams of Volmer-Heyrovsky reactions and Volmer-Tafel reactions using HL1, Mo2, and Te1 sites as representatives for each category of sites. As shown in Fig. S8(a), the active sites for Volmer reaction will keep catalytic activity for the Heyrovsky reaction. Thus, the Volmer reaction is the determining step for HER following Volmer-Heyrovsky reactions. In contrast, as shown in Fig. S8(b), The ΔG_H values of the Tafel reaction for all three adsorption sites are greater than the corresponding values for the Volmer reaction. Therefore, the calculated free energy diagrams indicate that Volmer-Heyrovsky reaction is the preferred pathway for HER, with the Volmer step being the critical step. Consequently the ΔG_H of the Volmer step can be used to evaluate the overall HER activity of the $MoTe_2$ boundary.

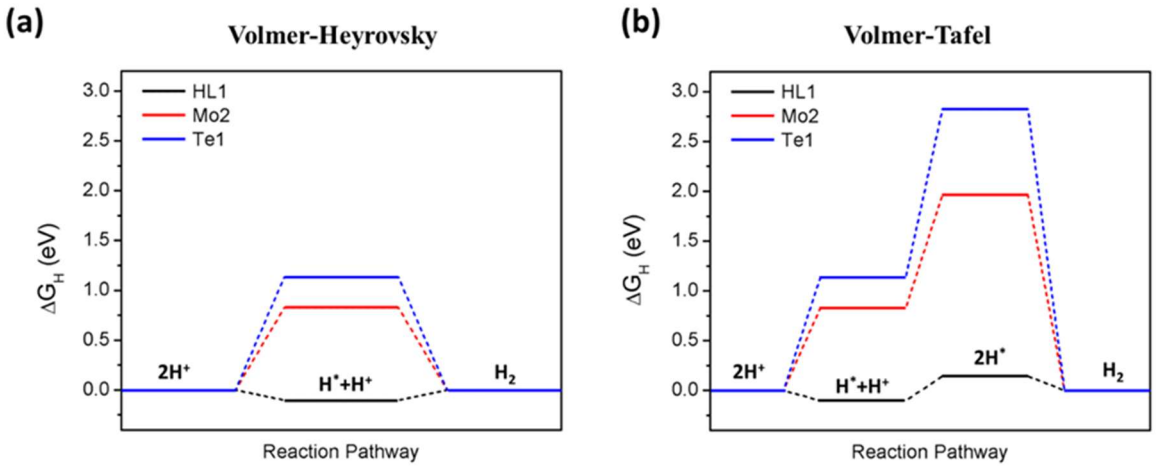

Fig. S8. Free energy diagram of the HER following (a) the Volmer−Heyrovsky pathway and (b) the Volmer−Tafel pathway at HL1, Mo2, and Te1 sites along the $MoTe_2$ phase boundaries.

S9. HER performance of few-layer $MoTe_2$ nanosheets

We have performed additional calculations to investigate the HER performance of few-layer $MoTe_2$ nanosheets. Fig. S9 presented the results on a double-layered $MoTe_2$ nanosheet containing phase boundaries, in comparison with the monolayer case. We can see that the ΔG_H values of different adsorption sites, i.e., HL, Mo, and Te sites in single- and double-layered $MoTe_2$ nanosheets are nearly identical (under the same H coverage, i.e., 100%), indicative of the catalytic activity in HER not altered by layer numbers. Three-layer $MoTe_2$ nanosheet model has also been constructed with benchmark calculations performed, which also confirmed no change in ΔG_H values at different adsorption sites.

The ignorable influence of layer number is likely attributed to the weak interlayer interaction (which is VdW in nature). Therefore, though our focus is on monolayer TMDCs, we believe the main conclusions would also apply to fewer-layer TMDC nanosheets.

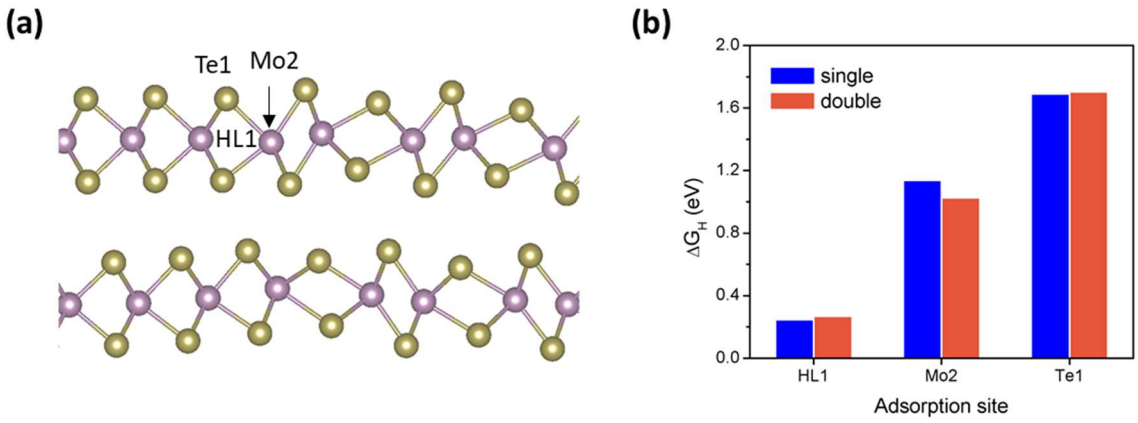

Fig. S9 (a) Side view of a double-layered $MoTe_2$ nanosheet containing phase boundaries in each layer, where Mo atoms are colored purple and Te atoms are colored brown. The three adsorption sites, selected as representatives and labeled as HL1, Mo2, and Te1, are indicated in the figure. (b) ΔG_H values at those sites in single-layered and double-layered $MoTe_2$.

S10. HER performance of other TMDC phase boundaries

We constructed $MoSe_2$ and WTe_2 phase boundaries, and selected three representative adsorption sites at the phase boundary (as well as their corresponding counterparts) to examine the HER activity (see Fig. S10(a)). As shown in Fig. S10(b), X1, HL1 and M1 sites at the basal plane of three pristine TMDCs exhibit similar high ΔG_H values, indicating inertness from pristine TMDC basal planes. On the other hand, the three sites, X1, HL1 and M1 at the phase boundary exhibit much lower ΔG_H values. This demonstrated that phase boundaries have similar enhancement effects to these TMDCs in terms of the HER activity. Therefore, the route of basal plane activation by phase boundaries is expected to work for different TMDCs.

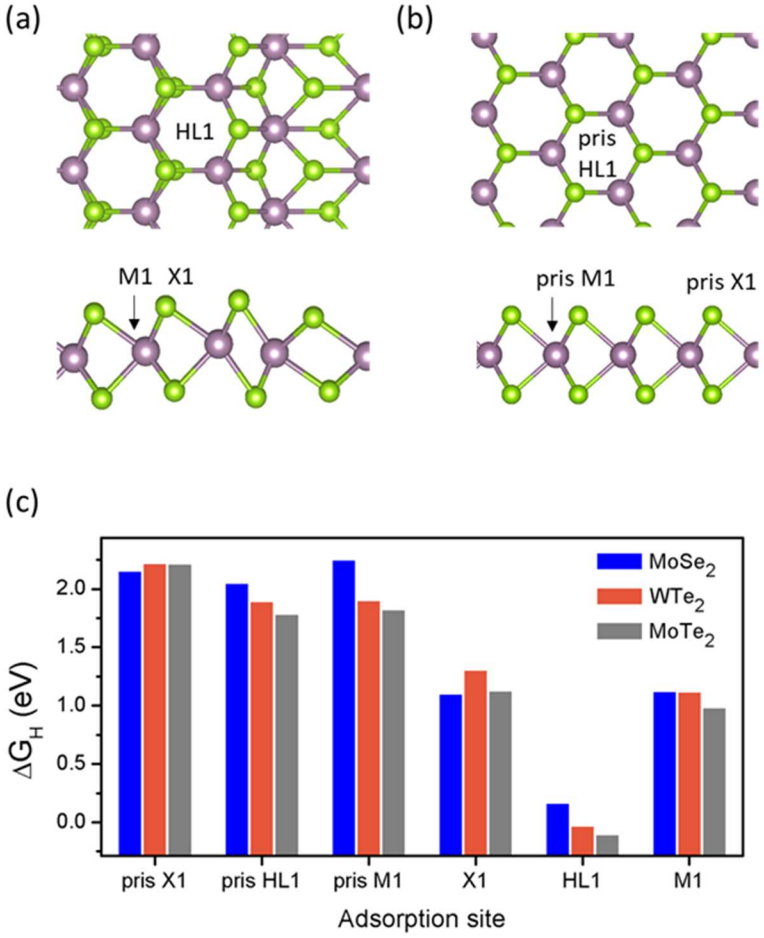

Fig. S10 (a) Representative adsorption sites in the TMDC phase boundary, labeled as HL1, M1 (metal site), and X1 (chalcogen site) respectively, as well as (b) their corresponding counterparts in the pristine TMDC basal plane, labeled as pris HL1, pris M1 (metal site), and pris X1 (chalcogen site) respectively. (c) ΔG_H values of X1, HL, M1 sites at $MoSe_2$, WTe_2, $MoTe_2$ phase boundaries, and at their corresponding counterparts in pristine TMDC basal planes.

S11. DOS of different Te sites in phase boundaries

Fig. S11 shows the DOS plots for different Te sites in phase boundaries.

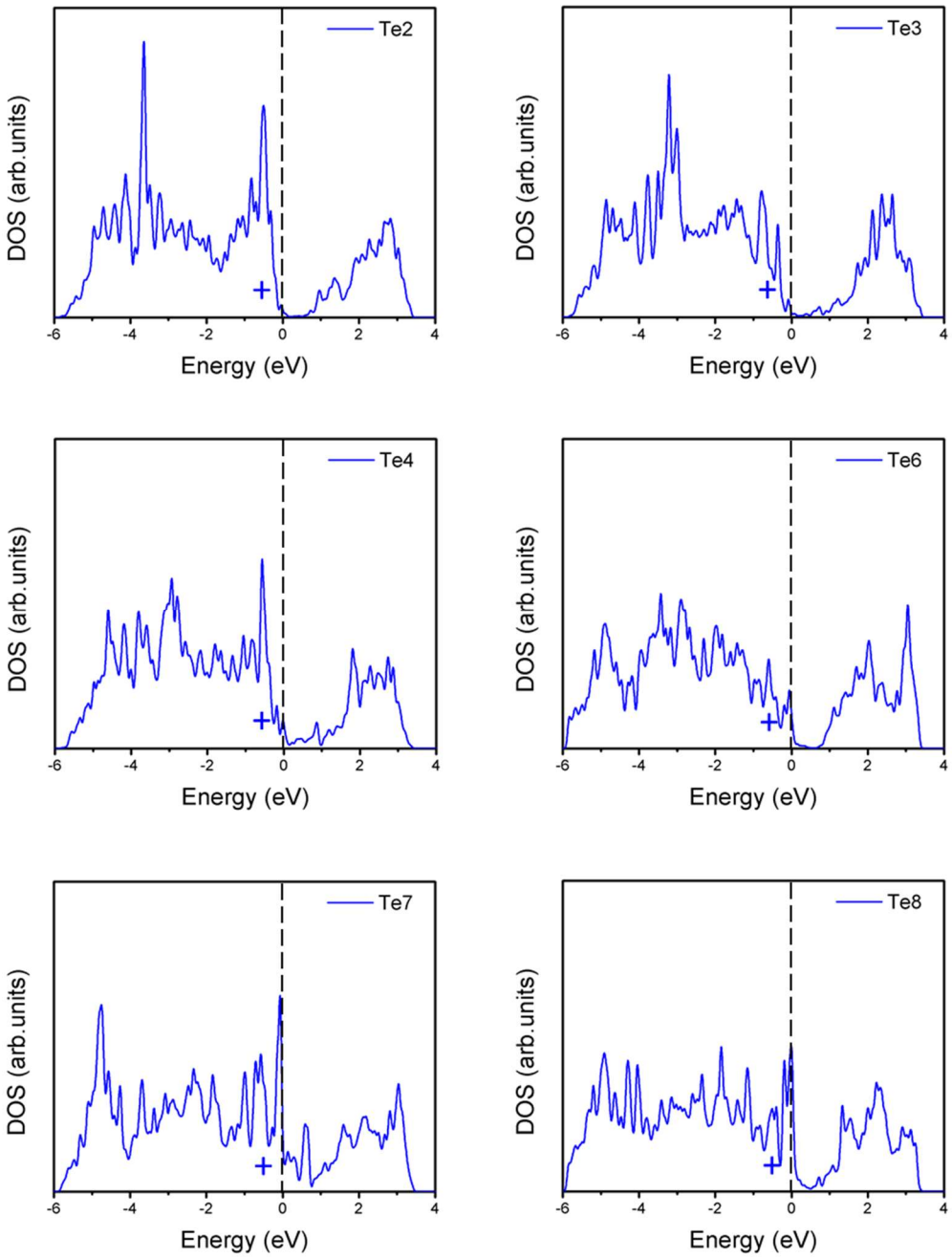

Fig. S11. Corresponding DOS plots of different Te sites (locations and configurations of those sites, please see Fig. 3(a) and (c)). The symbol "+" labels the position of Fermi-abundance center (D_F).

S12. The Fermi-abundance model for Mo sites

The calculated D_F of various Mo sites as a function of ΔG_H is shown in Fig. S12(a), which apparently does not show a linear trend. Therefore, the Fermi-abundance model fails to describe the HER activity of Mo atoms. As described in the main text, this is because hydrogen adsorption at a Mo site involves hydrogen interacting with more than just the Mo atom, while the Fermi-abundance model is essentially limited to describing the relationship between a hydrogen atom and a single adsorption site. Similarly the model breaks down for the case of the HL sites, where hydrogen atom forms bonding with three Mo atoms.

We also plotted the d-band center values[5] of Mo sites at the phase boundary as functions of ΔG_H. We can see that the d-band center values do not display any clear trend with respect to ΔG_H, indicating that d-band center theory being not applicable.

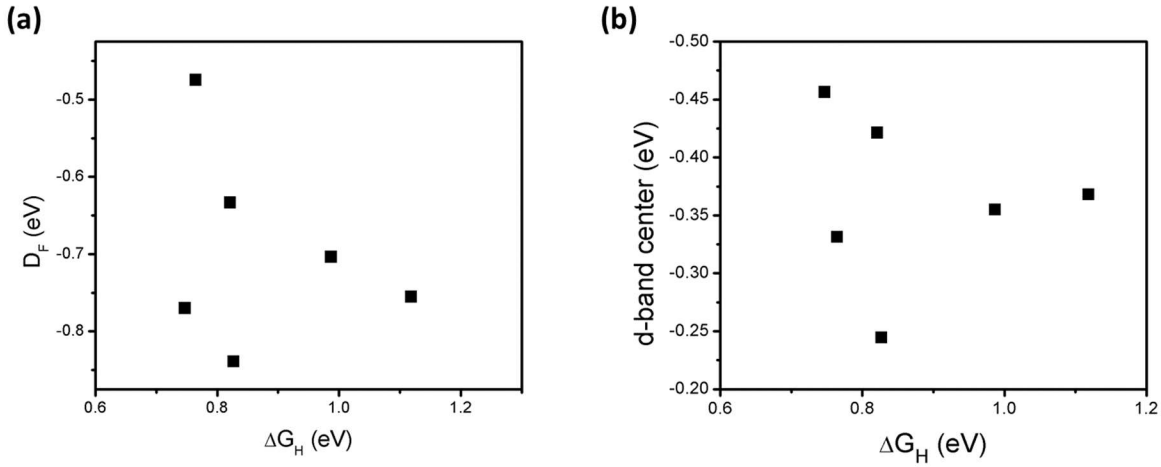

Fig. S12. Calculated (a) D_F and (b) d-band center of various Mo sites versus the corresponding ΔG_H values.

S13. Charge distribution at various adsorption sites along phase boundaries

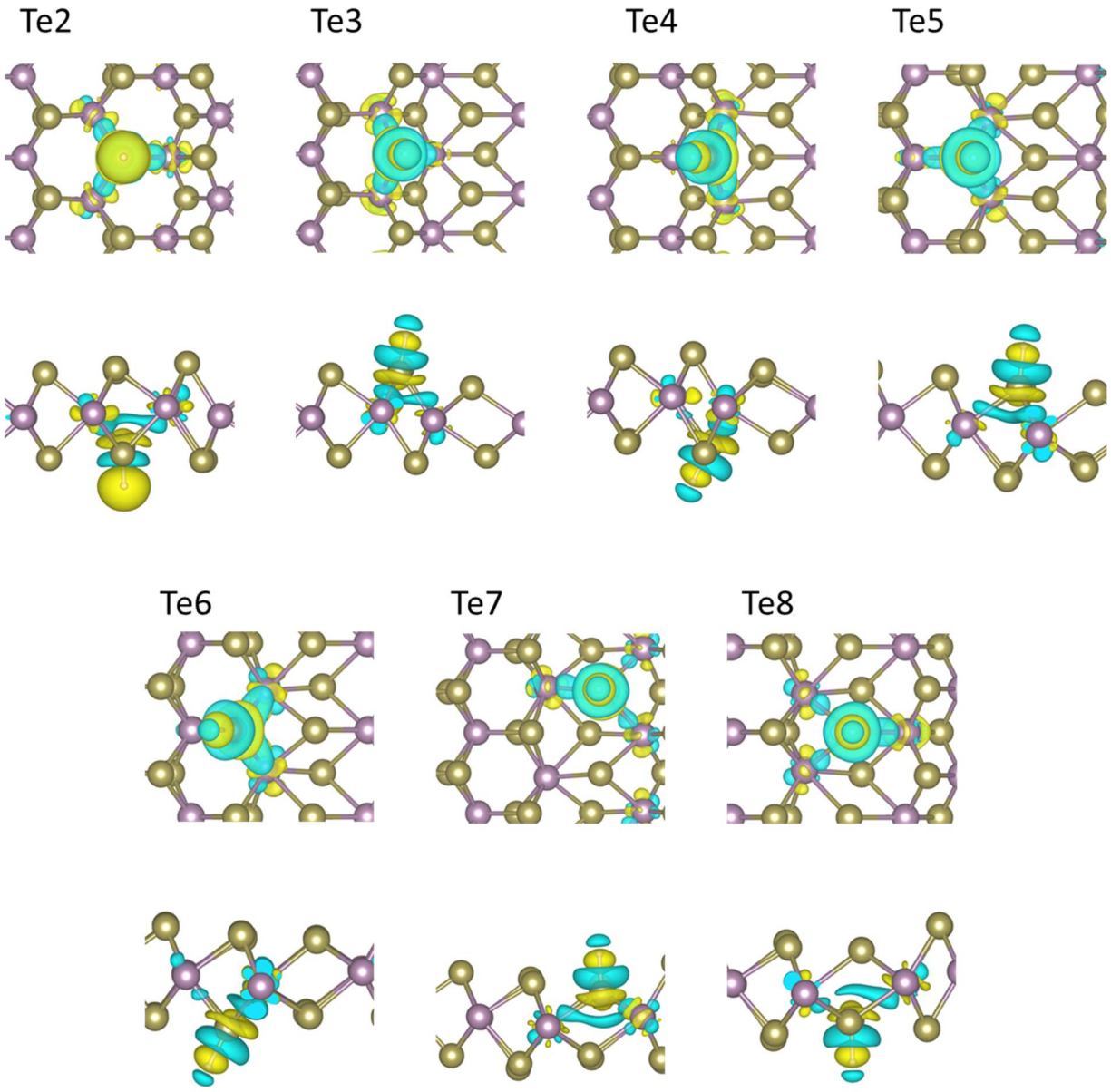

Fig. S13. Charge distribution at various Te sites in $MoTe_2$ phase boundaries.

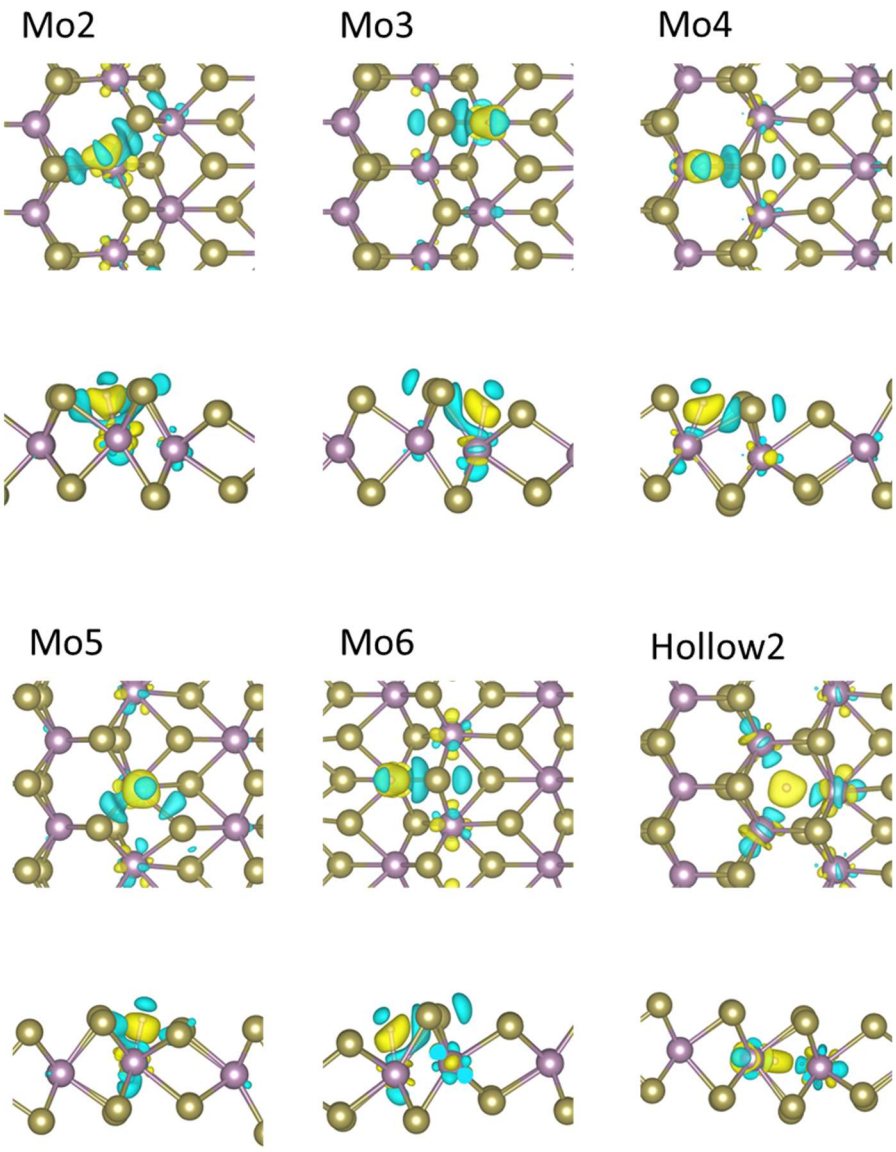

Fig. S14. Charge distribution at Mo and HL sites in $MoTe_2$ phase boundaries.

S14. DOS plots of various Mo sites

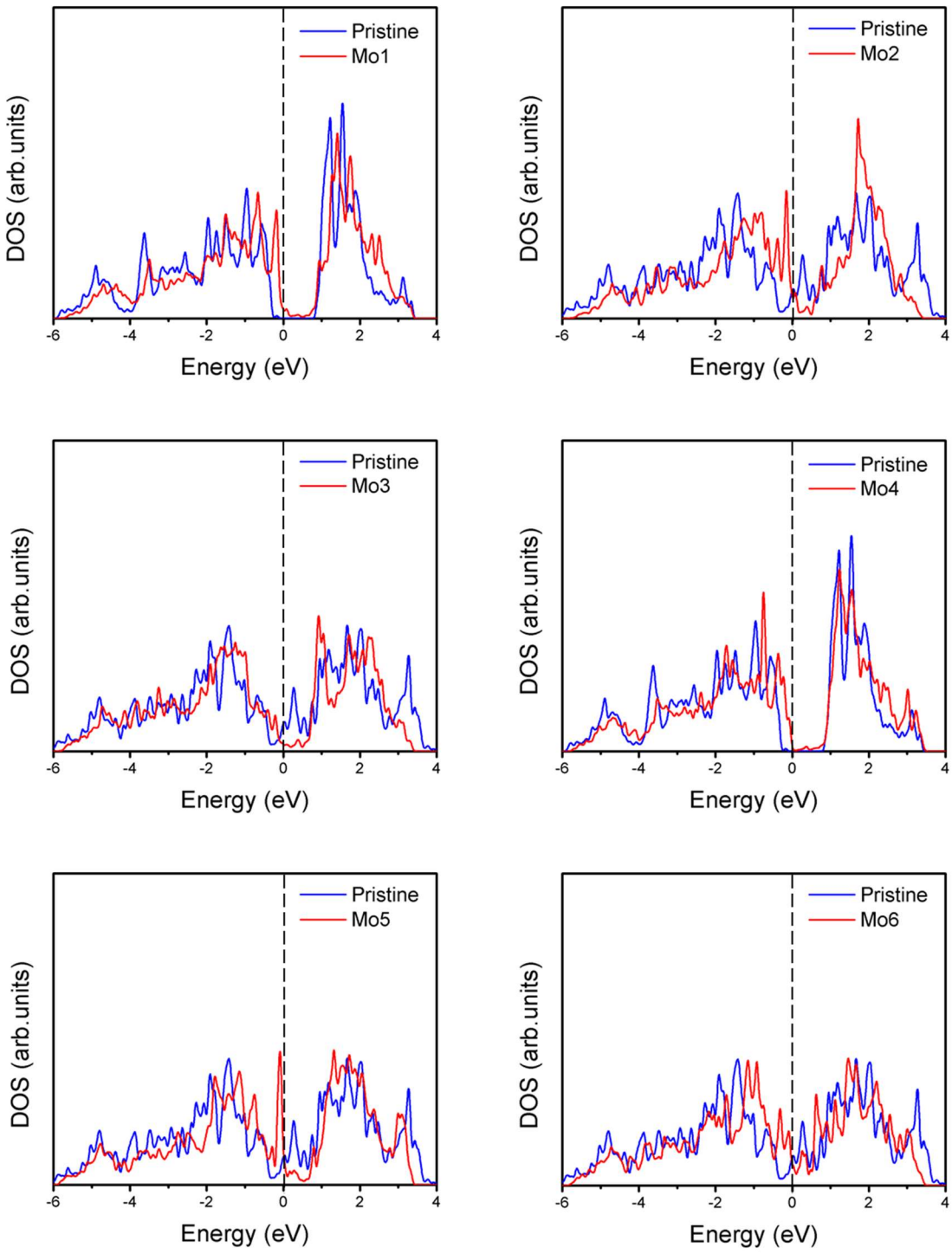

Fig. S15. DOS of Mo sites in phase boundaries in comparison with the Mo site in pristine $MoTe_2$ sites (locations and configurations of those sites, please see Fig. 3(a), (c) and Fig. S4).

S15. Projected DOS for d orbitals of Mo2 atoms

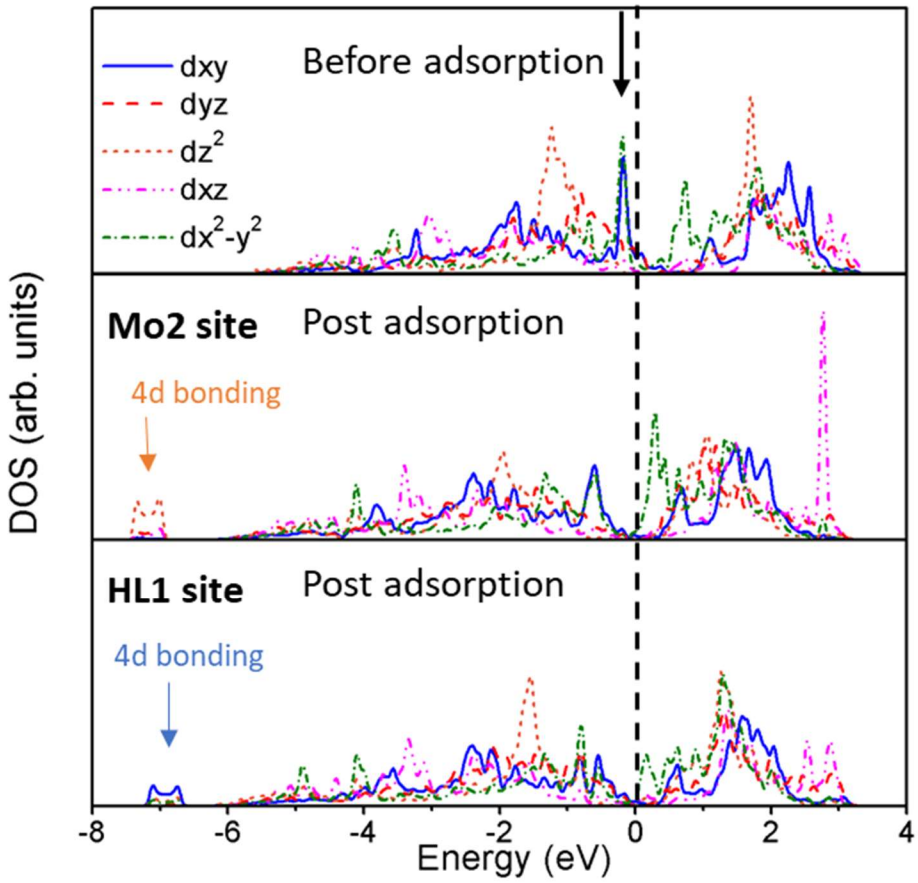

Fig. S16. Projected DOS (pDOS) plot for the d orbitals of the Mo2 atom along the $MoTe_2$ phase boundary, (top panel) before adsorption, after adsorption on Mo2 site, and after adsorption on HL1 site. Black arrow indicates the reinforcing states of dxy and $dx^2 - y^2$ orbitals near the Fermi level.

REFERENCES:

1. J. P. Perdew, K. Burke and M. Ernzerhof, *Physical Review Letters*, 1996, **77**, 3865-3868.
2. J. Heyd, G. E. Scuseria and M. Ernzerhof, *J. Chem. Phys.*, 2003, **118**, 8207.
3. A. Li, J. Pan, X. Dai and F. Ouyang, *Journal of Applied Physics*, 2019, **125**.
4. S. Zhou, J. Han, J. Sun and D. J. Srolovitz, *2D Materials*, 2017, **4**.
5. M. Mavrikakis, B. Hammer and J. K. Nørskov, *Physical Review Letters*, 1998, **81**, 2819-2822.